Regular Article - Experimental Physics

Intrinsic backgrounds from Rn and Kr in the XENON100 experiment

XENON Collaboration[1,⋆]

E. Aprile[1], J. Aalbers[2], F. Agostini[3,4], M. Alfonsi[5], F. D. Amaro[6], M. Anthony[1], F. Arneodo[7], P. Barrow[8], L. Baudis[8],
B. Bauermeister[9], M. L. Benabderrahmane[7], T. Berger[10], P. A. Breur[2], A. Brown[2], E. Brown[10], S. Bruenner[11],
G. Bruno[3], R. Budnik[12], L. Bütikofer[13,c], J. Calvén[9], J. M. R. Cardoso[6], M. Cervantes[14], D. Cichon[11,b],
D. Coderre[13], A. P. Colijn[2], J. Conrad[9,d], J. P. Cussonneau[15], M. P. Decowski[2], P. de Perio[1], P. Di Gangi[4],
A. Di Giovanni[7], S. Diglio[15], G. Eurin[11], J. Fei[16], A. D. Ferella[9], A. Fieguth[17], W. Fulgione[3,18], A. Gallo Rosso[3],
M. Galloway[8], F. Gao[1], M. Garbini[4], C. Geis[5], L. W. Goetzke[1], Z. Greene[1], C. Grignon[5], C. Hasterok[11],
E. Hogenbirk[2], R. Itay[12], B. Kaminsky[13,c], S. Kazama[8], G. Kessler[8], A. Kish[8], H. Landsman[12], R. F. Lang[14],
D. Lellouch[12], L. Levinson[12], Q. Lin[1], S. Lindemann[11,13,a], M. Lindner[11], F. Lombardi[16], J. A. M. Lopes[6,e],
A. Manfredini[12], I. Maris[7], T. Marrodán Undagoitia[11], J. Masbou[15], F. V. Massoli[4], D. Masson[14], D. Mayani[8],
M. Messina[1,7], K. Micheneau[15], A. Molinario[3], K. Morå[9], M. Murra[17], J. Naganoma[21], K. Ni[16], U. Oberlack[5],
P. Pakarha[8], B. Pelssers[9], R. Persiani[15], F. Piastra[8], J. Pienaar[14,19], M.-C. Piro[10], V. Pizzella[11], G. Plante[1],
N. Priel[12], D. Ramírez García[5,13], L. Rauch[11], S. Reichard[14], C. Reuter[8,14], A. Rizzo[1], N. Rupp[11],
J. M. F. dos Santos[6], G. Sartorelli[4], M. Scheibelhut[5], S. Schindler[5], J. Schreiner[11], M. Schumann[13],
L. Scotto Lavina[22], M. Selvi[4], P. Shagin[21], M. Silva[6], H. Simgen[11], M. Von Sivers[13,c], A. Stein[20], D. Thers[15],
A. Tiseni[2], G. Trinchero[18], C. Tunnell[2,19], M. Vargas[17], H. Wang[20], Z. Wang[3], M. Weber[1,11], Y. Wei[8,16],
C. Weinheimer[17], C. Wittweg[17], J. Wulf[8], J. Ye[16], Y. Zhang[1]

[1] Physics Department, Columbia University, New York, NY 10027, USA
[2] Nikhef and the University of Amsterdam, Science Park, 1098XG Amsterdam, Netherlands
[3] INFN-Laboratori Nazionali del Gran Sasso and Gran Sasso Science Institute, 67100 L'Aquila, Italy
[4] Department of Physics and Astrophysics, University of Bologna and INFN-Bologna, 40126 Bologna, Italy
[5] Institut für Physik & Exzellenzcluster PRISMA, Johannes Gutenberg-Universität Mainz, 55099 Mainz, Germany
[6] LIBPhys, Department of Physics, University of Coimbra, 3004-516 Coimbra, Portugal
[7] New York University Abu Dhabi, Abu Dhabi, United Arab Emirates
[8] Physik-Institut, University of Zurich, 8057 Zurich, Switzerland
[9] Oskar Klein Centre, Department of Physics, Stockholm University, AlbaNova, Stockholm SE-10691, Sweden
[10] Department of Physics, Applied Physics and Astronomy, Rensselaer Polytechnic Institute, Troy, NY 12180, USA
[11] Max-Planck-Institut für Kernphysik, 69117 Heidelberg, Germany
[12] Department of Particle Physics and Astrophysics, Weizmann Institute of Science, 7610001 Rehovot, Israel
[13] Physikalisches Institut, Universität Freiburg, 79104 Freiburg, Germany
[14] Department of Physics and Astronomy, Purdue University, West Lafayette, IN 47907, USA
[15] SUBATECH, IMT Atlantique, CNRS/IN2P3, Université de Nantes, 44307 Nantes, France
[16] Department of Physics, University of California, San Diego, CA 92093, USA
[17] Institut für Kernphysik, Westfälische Wilhelms-Universität Münster, 48149 Münster, Germany
[18] INFN-Torino and Osservatorio Astrofisico di Torino, 10125 Torino, Italy
[19] Department of Physics, Kavli Institute of Cosmological Physics, University of Chicago, Chicago, IL 60637, USA
[20] Physics & Astronomy Department, University of California, Los Angeles, CA 90095, USA
[21] Department of Physics and Astronomy, Rice University, Houston, TX 77005, USA
[22] LPNHE, Université Pierre et Marie Curie, Université Paris Diderot, CNRS/IN2P3, Paris 75252, France

⋆ e-mail: xenon@lngs.infn.it
a e-mail: sebastian.lindemann@physik.uni-freiburg.de
b e-mail: dominick.cichon@mpi-hd.mpg.de
c Also with Albert Einstein Center for Fundamental Physics, University
 of Bern, Switzerland

d Wallenberg Academy Fellow
e Also with Coimbra Engineering Institute, Coimbra, Portugal

Springer

Abstract   In this paper, we describe the XENON100 data analyses used to assess the target-intrinsic background sources radon (^{222}Rn), thoron (^{220}Rn) and krypton (^{85}Kr). We detail the event selections of high-energy alpha particles and decay-specific delayed coincidences. We derive distributions of the individual radionuclides inside the detector and quantify their abundances during the main three science runs of the experiment over a period of $\sim$ 4 years, from January 2010 to January 2014. We compare our results to external measurements of radon emanation and krypton concentrations where we find good agreement. We report an observed reduction in concentrations of radon daughters that we attribute to the plating-out of charged ions on the negatively biased cathode.

1 Introduction

Liquid noble gas detectors play an important role in rare-event search experiments looking for dark matter interactions or neutrinoless double beta decay [1]. One of their key features is ease of scalability. With larger target masses, external radioactivity can be better shielded through fiducialization. This is not the case for internal backgrounds that are intrinsic to the liquid gas target. First, these are medium- to long-lived radioisotopes of the target itself. For instance, liquid argon detectors need to take special care to avoid ^{39}Ar [2]. In the case of liquid xenon detectors, the two-neutrino double-beta emitter ^{136}Xe becomes relevant at the multi-ton scale [3]. Second, and more relevant for xenon detectors, are the radionuclides from radon and krypton. Both elements are inert gases that cannot be removed by established purification techniques based on hot gas purifiers commonly used in the field [4–7]. Radon and krypton dissolve in the liquid xenon target and cannot be excluded by standard fiducialization techniques which otherwise allow the rejection of background [5]. In this work we describe how krypton and radon backgrounds are assessed in the XENON100 experiment. Dark matter data from the three main XENON100 science runs (SRs), with exposure times of 101, 223 and 153 days each, are examined. The runs themselves and the corresponding detector conditions are outlined in Table 1 of [8].

2 The XENON100 detector

The XENON100 detector [5] is a cylindrical dual-phase time projection chamber (TPC) of 30.5 cm height and 30.6 cm diameter. It is located at the Laboratori Nazionali del Gran Sasso (LNGS) and uses about 62 kg of liquid xenon (LXe) as a target which is monitored by two arrays of photomultiplier tubes (PMTs), with one being at the top and one at

the bottom of the TPC. Its primary goal is to search for dark matter in the form of weakly interacting massive particles (WIMPs).

Incoming particles are detected via their interactions with the LXe, generating xenon scintillation photons (S1 signal) as well as ionization electrons. The electrons then drift towards the top of the TPC due to a homogeneous drift field applied across the LXe volume. At the top of the TPC, the electrons are accelerated into a region of gaseous xenon (GXe) by an extraction field. Due to the moving electrons interacting with the GXe, proportional scintillation photons are created (S2 signal) [9]. Both S1 and S2 signals, measured in photoelectrons (PE), are detected by the PMT arrays. The delay between the S1 and the S2 signals of an interaction, combined with the hit pattern of the S2 signal on the top array, allows the reconstruction of all 3 coordinates of the interaction vertex. The X and Y coordinates are defined relative to the TPC's central axis (where $X = Y = 0$) and are determined with a resolution of $\sigma_{X/Y} < 3$ mm. The Z coordinate has a resolution of $\sigma_Z < 0.3$ mm and is defined with respect to the liquid gas interface at the top ($Z = 0$) and the cathode electrode, which is used to create the drift field, at the bottom of the TPC ($Z = -30.5$ cm).

In addition, the S2/S1 ratio allows discrimination between nuclear recoils (NRs), which WIMPs are expected to induce, and electronic recoils (ERs), produced by γ-rays and β-particles. For example, in XENON100 WIMP analyses, 99.75 % of ERs can be rejected at the price of an energy-dependent NR acceptance of 30–50% by utilizing this feature [10]. As tails of the ER distribution contaminate the NR region, it is of paramount importance to measure the abundance of ^{222}Rn and ^{85}Kr and to estimate their impact on the detector's sensitivity to WIMP interactions.

3 Radon and thoron

The decays of ^{222}Rn (radon) and ^{220}Rn (thoron), as well as their daughters, are illustrated in Fig. 1 with the half-lives, $\mathcal{Q}$-values and branching ratios used throughout this work [11]. Radon and thoron are produced in the decay chains of the primordial nuclides ^{238}U and ^{232}Th, respectively. Both of these nuclides are present, at least at trace level, in all materials, making it necessary to carefully screen and select all detector components [12]. The radon concentration of the air underground at LNGS, emanating from the surrounding rock, has been found to be of $\mathcal{O}(100$ Bq/m^3) [10]. For this reason, the inner cavity of the detector's shield is continuously flushed with boil-off nitrogen [5], minimizing the amount of ambient radon and thoron that could potentially enter.

Levels of radon and thoron inside the LXe target of XENON100 are determined by the emanation of either iso-

tope from surfaces inside the detector and the xenon purification system. Additionally, one period before SR1 and two periods during SR2 and SR3, were identified where air leaks of $\mathcal{O}(10^{-3}$ mbar l/s) and $\mathcal{O}(10^{-5}$ mbar l/s), respectively, developed at the purification system's diaphragm pump, leading to a variation of the radon background over time (see [13] and Sec. 3.3).

After entering the LXe, radon and thoron are able to reach the fiducial volume used for the WIMP search via diffusion and convection [14]. As a consequence, β-decaying daughter nuclides of both isotopes can contribute to the low-energy ER background. Contributions from α-decays are not relevant because the involved α-particle energies are two orders of magnitude larger than the energies expected from WIMP-induced NRs, which are at $\mathcal{O}(10\,\text{keV})$ [10].

Some of the progeny of the chains' nuclei have short half-lives compared to the event window of XENON100, which has a length of 400 μs and is centered on the triggering signal [5]. This aspect results in two decays being recorded within the same event (delayed coincidence signature). An example for this are decays of ^{214}Bi (radon chain) and ^{212}Bi (thoron chain) which are followed by the decays of their polonium daughters (BiPo coincidence). This causes multiple S1 and S2 signals to be present in an event, making it possible to identify and reject them (see Sec. 3.2).

Of the β-decaying nuclides in either chain, many have a significant likelihood of decaying under prompt emission of γ-rays, which gives the same kind of signature as mentioned above. However, certain β-decaying nuclides from either chain are able to decay without γ-ray emission. If they are well-separated in time from accompanying decays, they are very likely to elude identification. Such nuclides are ^{214}Pb, ^{210}Pb (radon chain) and ^{212}Pb (thoron chain).
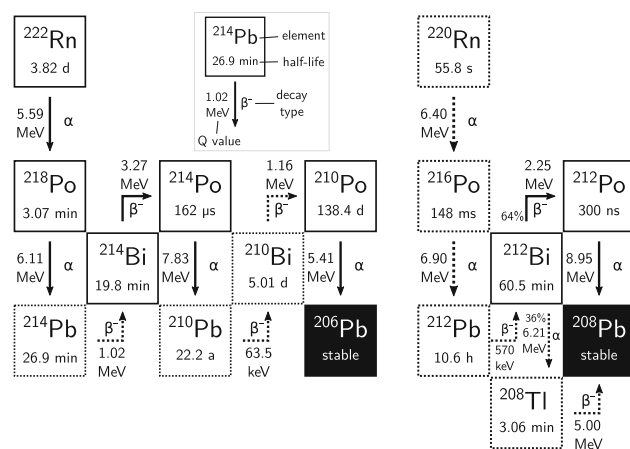

Fig. 1 Illustrations of the ^{222}Rn (radon) and ^{220}Rn (thoron) chains (ignoring decay modes with a branching ratio $\leq 0.1\%$). Half-lives, branching ratios and $\mathcal{Q}$-values are taken from [11]. Solid boxes mark the isotopes that are quantified in this work

Radon and thoron concentrations in the LXe target can be inferred by selecting and counting events from decays of their chains. Especially suited for this task are α-decays, as they produce large, monoenergetic signals resulting in a distinct event signature. Another explicit signature is the BiPo delayed coincidence as outlined above. This coincidence has already been successfully utilized by, for instance, the Borexino and SuperNEMO collaborations for estimating radioactive background levels inside their detectors [15,16] and by the XENON collaboration for assessing the suitability of a thoron source for calibrating tonne-scale LXe detectors [14]. The focus of this section is to describe the selection of α-decays and BiPo events. Results thereof are presented in Sec. 3.3.

3.1 Alpha event selection

For the analysis of α-decaying nuclides in XENON100, ^{222}Rn and ^{218}Po are used because they are the cleanest α populations available as explained further below. ^{214}Po is covered in Sec. 3.2 as part of the BiPo coincidence.

To select α-decays, a set of cuts, based on criteria described in [10,17], is applied to the data. We require at least one S1 signal with a minimum of two PMTs in coincidence. Any secondary S1 signal has to be below 1600 PE (motivated in [17]) to avoid decay pileup and multi-scatters. In addition, at least one S2 signal must be present with at least 25 % of its area observed by the top PMT array to reject misidentified signals. Due to the large signal sizes of α-decays, which are found to be of $\mathcal{O}(10^4\,\text{PE})$ for S1s and $\mathcal{O}(10^5\,\text{PE})$ for S2s, acceptance losses due to the above mentioned cuts are considered to be negligible.

Finally, the detector volume used for this analysis is restricted to $R = \sqrt{X^2 + Y^2} < 135$ mm and 10 mm $< Z <$ 260 mm ($\hateq 40.5$ kg LXe or 65.3 % of the active volume). This excludes regions close to the TPC walls, which suffer from reduced light and charge collection efficiencies, and regions with insufficient separation between ^{222}Rn and ^{218}Po.

A potential ^{210}Po population close to the PTFE wall enclosing the TPC is also selected for further studies. Selection criteria are the same as above, with the following differences: $R \geq 135$ mm is required, and the largest S2 signal must be smaller than 8×10^4 PE. The latter criterion is motivated by the observation of S2 signals well below those seen from ^{222}Rn and ^{218}Po for wall population events. Reduced S2 signals correspond to charge losses which can result from, for example, decays happening close to or within the walls. In the latter case, decay products can still enter the TPC, but lose energy in the process as they need to traverse the wall material. The S1 signal cannot be used as the only parameter for nuclide discrimination in this case, as the detector's energy resolution is insufficient to separate the peaks of ^{222}Rn and ^{210}Po in the S1 spectrum (see Fig. 2).
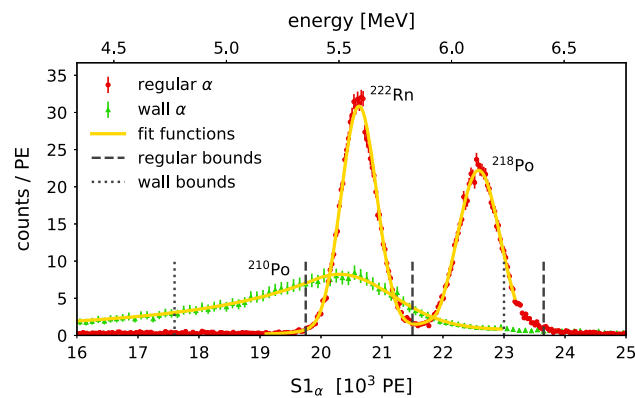
Fig. 2 Corrected $S1_\alpha$ spectra (SR1). The left peak of the regular α selection spectrum (red, circular markers) is attributed to ^{222}Rn, the right one to ^{218}Po, with their bounds (3σ intervals) indicated by dashed lines. The tailing peak in the wall selection spectrum (green, triangular markers) is considered to belong to ^{210}Po and has its bounds indicated by dotted lines

The largest S1 and S2 signals are interpreted as belonging to an α-decay and are correspondingly named $S1_\alpha$ and $S2_\alpha$. A position-dependent area correction for α-decays [17] is applied to $S1_\alpha$ in order to account for PMT saturation, which affects both the observed signal size and position reconstruction. Looking at the corrected $S1_\alpha$ spectrum for events happening at $R < 135$ mm (Fig. 2, red circular markers), we identify two peaks, which are attributed to the α-decays of ^{222}Rn and ^{218}Po, respectively.

To determine peak positions and extents while accounting for slight tailing, we fit a sum of two Crystal Ball functions (defined in equation (F-1) of [18]) and a constant to the peaks. Events are classified as containing a ^{222}Rn or ^{218}Po decay if the area of their $S1_\alpha$ is within 3σ of the respective peak mean (bounds as shown in Fig. 2). This choice is valid as the peaks are, in good approximation, symmetric. Fits are done separately for each SR due to changes of detector parameters affecting positions and widths of both peaks [8]. In all SRs, the peak bounds determined according to this method do either not overlap, or overlap negligibly. In the latter case, the bound separating both peaks is determined by the arithmetic mean of the overlapping bounds in order to ensure events to be attributed to a single peak only. Leakage of the peaks beyond the boundaries assigned to them are estimated to be $< 1\%$ and are thus considered negligible. For consistency, the same procedure is utilized for the wall population, as it also shows a peak in the S1 spectrum (Fig. 2, green triangular markers), using a single Crystal Ball function plus a constant for fitting.

In the thoron chain, the number of α-decays from ^{220}Rn and ^{216}Po can, in principle, be inferred from the $S1_\alpha$ spectrum via peak fitting (see [19]). However, in the XENON100 background, the ^{218}Po peak overlaps the ^{220}Rn peak region due to insufficient energy resolution. In addition, there is no

indication of ^{216}Po being present in the $S1_\alpha$ spectrum of the fiducial volume used, while, at the same time, it is negligible in the rest of the sensitive volume compared to the wall population. As thus no direct evidence of them exists in the fiducial volume, ^{220}Rn and ^{216}Po are not taken into account in this analysis, even though they are present in the detector as demonstrated by ^{212}Po being measured, which belongs to the nuclei discussed in detail in the following section.

3.2 BiPo event selection

The decays of ^{214}Bi and ^{212}Bi are often recorded within the same event as the decays of their daughter nuclei, ^{214}Po and ^{212}Po. This is due to the short half-life of the polonium isotopes compared to the event window recorded by the XENON100 data acquisition system. The S1 signals generated by the β decays of the bismuth isotopes ($S1_\beta$) are smaller than those generated by the α-decays of the polonium daughters ($S1_\alpha$), because the β-decay $\mathscr{Q}$-values (see Fig. 1) and ionization densities are lower than those of the α-decays [20].

The result is a delayed coincidence signature of one S1 signal being followed by a larger one. For selecting such events, we require at least two S1 signals with at least twofold PMT coincidence and the correct time order ($S1_\beta$ before $S1_\alpha$). Both signals need to be larger than 200 PE and $S1_\alpha$ has to pass a data quality cut on the fraction of its area observed by the top PMT array to reject signals seen almost exclusively by the bottom array. Such a signal topology is virtually impossible to occur for an α-decay happening inside the TPC due to the large amounts of scintillation photons generated (see Sec. 3.1).

In order to distinguish delayed coincidences from Bi and Po decays (called BiPos in the following) from either chain additional constraints are applied exploiting the fact that ^{212}Po has a much shorter half-life than ^{214}Po ($T_{1/2} = 300$ ns vs. $T_{1/2} = 162$ μs). ^{214}BiPos are selected by requiring $S1_\alpha$ to occur at least 7 μs after $S1_\beta$, which removes more than 99.99% of ^{212}BiPo events. For ^{212}BiPos, the time difference has to be between 0.5 μs and 2 μs. The lower bound ensures that both signals are individually identified with $\sim 100\%$ efficiency by the data processor, while the upper bound removes about 99% of ^{214}BiPo events.

Due to the possibility of γ-radiation accompanying the Bi-decays, the $S2_\alpha$ signal falling outside the event window, and signal losses because of the spatial distribution of events as detailed in Sec. 3.3, no constraints are required on the number of S2 signals and their parameters. In fact, as the number of S2 signals is expected to vary and event reconstruction is not optimized for pairing S1 and S2 signals when multiple physical interactions are present, signal matching has to be done separately. A match requires the absolute time difference between a pair of S2 signals to be within ~ 1 μs of

the one between the S1 signals (detailed in [21]). The S2 which occurs earlier is assigned to $S1_\beta$. If no match is found, the largest S2 is assigned to $S1_\beta$. We then recalculate positions and signal corrections (for $S1_\alpha$ and those mentioned in [5]) for each event, as both depend on pairing S1 with S2 signals. Events without any S2 signal are not rejected, but are assumed to have occurred in a charge-insensitive region such as below the cathode, with a set of default coordinates assigned to them ($R = 0$ cm, $Z = -30.5$ cm).

The data processor does not search for S1 signals occurring after a sufficiently large S2 signal within the same event [5]. This behavior is intentional as the processor has been developed for the analysis of single interaction events. However, this reduces the acceptance of the BiPo event selection because the $S1_\alpha$ signal might occur after the first S2 signal of the Bi-decay which happens after $S1_\beta$ within the maximum drift time of 176 μs [5]. This loss in acceptance as well as the one resulting from the finite size of the event window is accounted for by summing up weights ε for each BiPo event, defined by

$$\varepsilon^{-1} = \exp(-\lambda\,\Delta t_{min}) - \exp(-\lambda\,\Delta t). \tag{1}$$

λ is the decay constant of the corresponding polonium isotope, Δt is the time difference between $S1_\beta$ and the first S2 peak (or the end of the event window, if no S2 is present), and Δt_{min} is the minimum time difference between $S1_\alpha$ and $S1_\beta$ allowed by the selection criteria. Thus, the right side of equation (1) is the probability of a polonium decay to occur within the given constraints in time.

Acceptance losses caused by the $S1_\beta$ size criterion, however, cannot be reliably predicted without depending on measured ^{222}Rn and ^{220}Rn rates. This is caused by events that happen on the cathode, whose S1 signals are shadowed by the cathode grid which results in a modification of the expected $S1_\beta$ spectrum. The relevance of cathode events is explained in the following section. Losses induced by other quality cuts are negligible.

3.3 Results and discussion

The rate evolution of each decay is shown in Fig. 3. To verify that the selected event populations represent the correct nuclei, an exponential decay plus a constant offset is fitted to the rate decrease of ^{222}Rn that is observed during the two months of SR1 (Fig. 3, top left). A small air leak was closed before this period, resulting in the decay of the excess radon which is visible in the rate evolution.

The half-life given by the fit is $T_{1/2} = (3.81 \pm 0.12)$ d, which is in perfect agreement with the literature value for ^{222}Rn ($T_{1/2} = 3.82$ d). In addition, the relative positions of the peaks in the $S1_\alpha$ spectrum match the expectations given by the $\mathscr{Q}$-values of the individual decays, with a constant

light yield of ~ 3.7 PE/keV observed for all nuclides. Furthermore, the rates assigned to ^{222}Rn, ^{218}Po and ^{214}BiPo (radon chain) correlate with each other, while no correlation with the rates from ^{212}BiPo (thoron chain) and ^{210}Po (radon chain) can be seen. While the latter is also part of the radon chain, secular equilibrium is broken due to the long half-life of ^{210}Pb ($T_{1/2} = 22.2$ y). While thoron can also enter the detector via leaks, it has a much shorter half-life ($T_{1/2} = 55.8$ s) than ^{222}Rn, which results in a large suppression as it is more likely that it decays before reaching the TPC [14].

The condition on the S2 peak size introduced to select decays originating from the TPC's PTFE walls does not specifically select ^{210}Po. However, considering that its rate is not correlated with the remainder of the radon chain, and taking into account similar observations made by the LUX experiment [22], we conclude that the wall population indeed consists of ^{210}Po. The spatial distribution that includes it (see Fig. 4) shows that it is located almost exclusively at $R^2 > 200$ cm^2, while the largest fiducial volume used for XENON100 WIMP analyses requires $R^2 < 200$ cm^2 among other constraints [23]. For $R^2 < 180$ mm^2, a small number of events, likely caused by ^{222}Rn and ^{218}Po leakage, can be seen. However, it is evident that these events are negligible compared to those happening at $R^2 \geq 180$ mm^2 as well as to those belonging to ^{222}Rn and ^{218}Po.

Computing the average specific rates (Table 1) yields (48.0 ± 0.4) μBq/kg, (64.3 ± 0.4) μBq/kg and (68.3 ± 0.4) μBq/kg for ^{222}Rn in SR1 to SR3 respectively. Periods of increased average rates and fluctuations are observed in SR2 and SR3. These increases are caused by tiny air leaks in the diaphragm pump used in the xenon purification system, leading to a correlation of the ^{222}Rn rates inside and outside of the detector [13]. Restricting the rate average to periods not affected by a leak gives (38.3 ± 0.4) μBq/kg (SR1) and (41.8 ± 0.9) μBq/kg (SR3). We thus conclude that constant emanation of radon from detector materials results in a base rate of, on average, 40 μBq/kg.

A direct measurement of the ^{222}Rn emanation at room temperature by means of miniaturized proportional counters was performed in summer 2012 between SR2 and SR3 [24]. It resulted in (9.3 ± 1.0) mBq and (2.6 ± 0.5) mBq being measured for the XENON100 detector and gas system, respectively, leading to an expected specific rate of (74 ± 7) μBq/kg assuming homogeneous mixing of ^{222}Rn in the full LXe inventory. Inside the TPC, the assumption of homogeneous mixing is valid, with the exception of ^{210}Po (Fig. 4). The apparent decrease of ^{214}BiPo events towards the top of the TPC is caused by losses induced by the peak finding algorithm as explained in Sec. 3.2 and by γ-rays, which accompany the ^{214}Bi decay, scattering off the LXe at a different position than the original decay. Measurements with an external ^{222}Rn source suggest, that the homogeneous
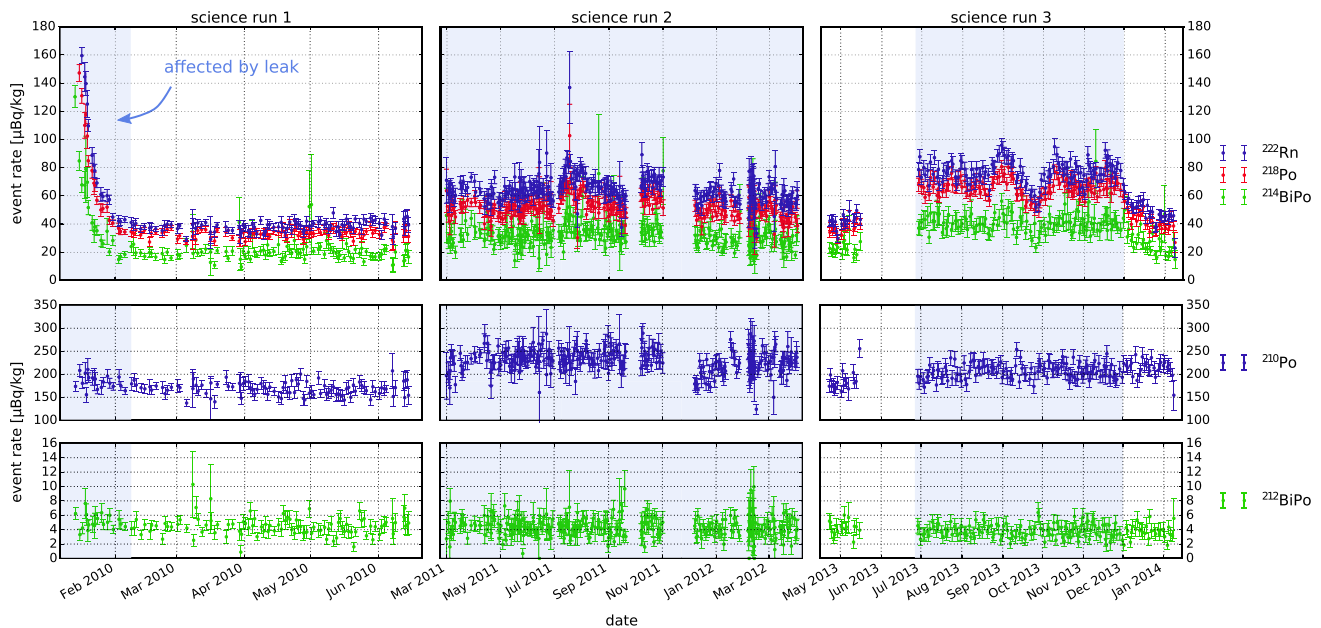
Fig. 3 Radon event rates during the three SRs. Before starting SR1, ^{222}Rn entered the detector via an air leak which was subsequently closed. The decay of this additional radon contribution is clearly visible in the rates, and the decay constant is compatible with expectations from literature values (see text for more details). Note the rate correlation among ^{222}Rn, ^{218}Po (selected by α-counting) and ^{214}BiPos (selected by delayed coincidence analysis) which are shown in the top row. The rates of ^{212}BiPos (delayed coincidence analysis) and ^{210}Po (wall event selection), shown in the bottom rows, do not correlate with them. Regions affected by a leak are shaded in blue. Mismatches between rates of the ^{222}Rn chain nuclides are explained in the text
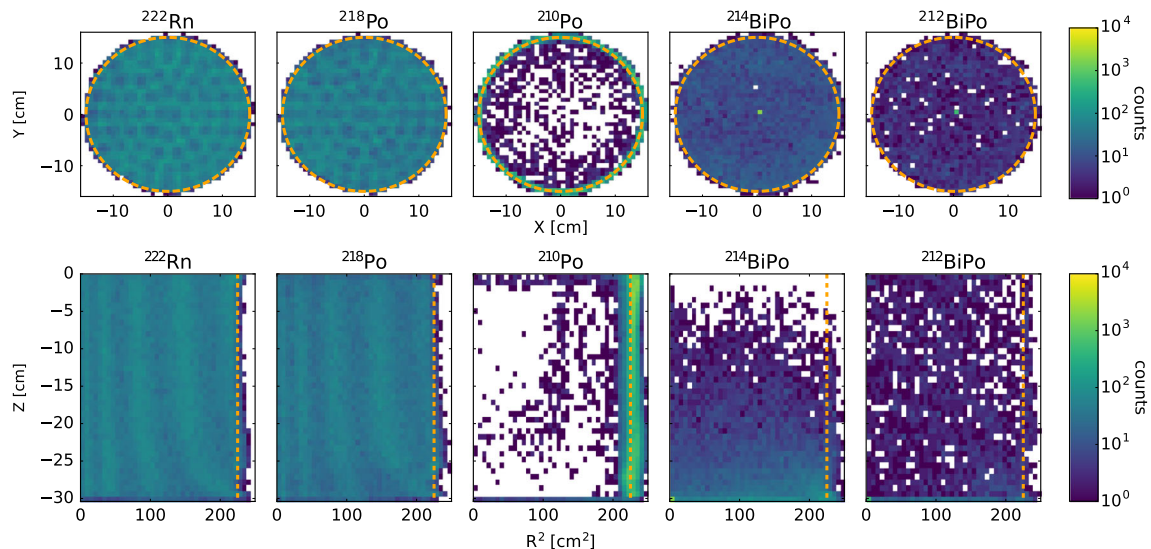

Fig. 4 Spatial distributions of the radon populations identified in XENON100. Dashed lines indicate the TPC's radius. For ^{222}Rn and ^{218}Po, the main S2 signal is required to be larger than 80000 PE to separate both from ^{210}Po at $R > 135$ mm (losses introduced by this cut are negligible at smaller radii). (Top) XY distributions. Due to vertex reconstruction artifacts caused by PMT saturation, the structure of the top PMT array is visible in the ^{222}Rn and ^{218}Po data. (Bottom) $R^2 Z$ distributions. Only events whose reconstructed Z is within the TPC's actual height are shown. The same reconstruction artifacts as for the top plots are visible in the ^{222}Rn and ^{218}Po distributions. The number of ^{214}BiPo events seems to diminish toward the top of the TPC, but this is actually an artifact induced by the peak finder peculiarities described in Sec. 3.2 and by multi-scatters induced by γ-rays which accompany the ^{214}Bi decay [17]

admixing of radon throughout the entire LXe inventory takes place within a few hours [19]. The environmental conditions of the direct measurements with proportional counters differed from the standard operation conditions, as the detector and gas system were at different temperatures and exposed to nitrogen or helium, respectively. Both the increased temper-

Table 1 Average specific rates for all SRs (statistical errors only). The leak period of SR1 ends on February 7, 2010, and the leak period of SR3 lasts from June 27, 2013, to December 1, 2013. Note that the ^{210}Po rate concentration is large compared to the other nuclides because it is concentrated at the PTFE wall enclosing the TPC

Type	Rate [µBq/kg]					
	SR1	SR1 (aft. leak)	SR2	SR3	SR3 (bef. leak)	SR3 (dur. leak)
^{222}Rn	48.0 ± 0.4	38.3 ± 0.4	64.3 ± 0.4	68.3 ± 0.4	41.8 ± 0.9	76.7 ± 0.4
^{218}Po	41.0 ± 0.4	33.4 ± 0.4	52.2 ± 0.3	59.0 ± 0.3	37.1 ± 0.9	66.1 ± 0.4
^{210}Po	171.0 ± 1.4	168.4 ± 1.5	229.9 ± 1.3	205.6 ± 1.2	185 ± 4	206.7 ± 1.4
^{214}BiPo	24.8 ± 0.6	20.5 ± 0.6	32.8 ± 0.5	36.9 ± 0.5	22.9 ± 1.2	41.1 ± 0.6
^{212}BiPo	4.59 ± 0.11	4.48 ± 0.12	4.41 ± 0.08	3.88 ± 0.08	4.3 ± 0.3	3.86 ± 0.09

ature and reduced stopping power are known to impact the emanation rate of ^{222}Rn (for example, see [25,26]) and we consider the direct measurement to be a weak confirmation of our results.

A priori, we expect the radon chain from ^{222}Rn to ^{214}Po to be in secular equilibrium, as the longest-lived daughter nuclide in this part of the chain, ^{214}Pb, has a half-life of 26.9 min (Fig. 1). This is short compared to both the time scales of the SRs, which lasted for several months (Fig. 3), and the time scale of the target purification, which is about 5 days per revolution. However, we observe only about 50 % of the expected amount of ^{214}BiPo events and about 86 % of ^{218}Po events (Table 1). Acceptance losses due to cuts are negligible for the α-events from ^{218}Po because of their high-energy signature. Thus, we have to consider additional causes for this mismatch. The most appealing one is radon daughters plating out onto the cathode due to convection and drift in the electric field. Radon daughters which remain ionized were, for example, observed in the EXO-200 TPC [27], and plating of radon progeny onto the cathode of a LXe TPC has already been reported by the ZEPLIN-III collaboration [28]. The precise motivation for the plate-out hypothesis is the observation of a surplus of events in the cathode region for ^{214}BiPos and ^{212}BiPos (Fig. 4), which is visible even when rejecting events without a proper S2 signal (which we assign to $Z = -30.5$ cm, the height of the cathode, by default). In addition, it has been observed in ^{220}Rn calibration data, that the drift field affects the motion of ^{220}Rn daughters inside the detector [14]. While nuclide velocities inside the TPC are dominated by convection, which contributes up to $\sim$ 5 mm/s to up-/downward motion along the Z axis, a constant contribution of $\sim$ 1 mm/s towards the cathode is observed which is attributed to the drift field (500–533 V/cm depending on the SR [8]). As a consequence of the plate-out, decays happening on the cathode are shadowed, leading to losses in the S1 signal and thus a lower acceptance of BiPo and ^{218}Po events.

No cathode accumulation is seen in the ^{218}Po distribution. Such an effect could be hidden due to the reduced discrimination power at the bottom of the TPC between ^{218}Po and ^{222}Rn (see Sec. 3.1). In addition, the effect on ^{214}BiPos is assumed

to be enhanced because of the repeated chance of collecting ionized daughters with every decay. A larger fraction of ^{214}Bi remaining ionized compared to ^{218}Po, as suggested in [27], might also play a role.

^{210}Po rates are larger compared to those of other radon chain nuclides by a factor of $\sim$ 4.2 in the outermost part of the detector in periods not affected by a leak. However, one has to take into account that the volume within which ^{210}Po is selected is by a factor of $\sim$ 4.5 smaller than a volume without any requirement on R (Sec. 3.1). Averaging the ^{210}Po activity without constraining R gives, for instance, (38.6 ± 0.3) µBq/kg in SR1. Because this rate is still larger than the one observed for ^{214}BiPos and does not correlate with rates of preceding chain decays, we assume surface contamination of the PTFE walls due to air exposure during TPC assembly to be the origin of the ^{210}Po population (analogous to observations made in [29]). Under this assumption, we find a ^{210}Po activity per unit area of PTFE in the range from 0.6–0.9 µBq/cm^2.

4 Krypton

Natural krypton is present at the parts-per-billion (ppb) level in commercially available xenon produced in air separation plants. It contains the radioisotope ^{85}Kr, which is an almost pure beta emitter and has a relatively long half-life of 10.76 years. Krypton spreads throughout the liquid xenon target where it can induce low-energy events that may leak into the WIMP search region. To mitigate the ^{85}Kr-induced background, the xenon target typically is purified by means of adsorption or distillation before starting a measurement [30–33]. However, re-contamination due to even tiny air leaks readily increases the concentration of ^{85}Kr.

Natural sources result in a constant equilibrium content of 0.09 PBq ^{85}Kr in the atmosphere [34]. In addition, ^{85}Kr is produced alongside plutonium in spent nuclear fuel and irradiated breeding targets. The noble gas remains therein until it is released by nuclear fuel reprocessing facilities during the extraction of plutonium. These anthropogenic sources

increase the atmospheric concentration of ^{85}Kr by orders of magnitude [35]. In present-day northern atmosphere, the activity of ^{85}Kr is approximately 1.4 Bq/m^3 [36,37]. This number roughly corresponds to a relative isotopic abundance of ^{85}Kr/^{nat}Kr = 2 × 10^{-11} mol/mol [38]. However, the ^{85}Kr concentration varies across both time and space due to location and duty cycles of reprocessing plants as well as region-specific meteorological conditions [35]. To our knowledge, no atmospheric ^{85}Kr monitoring data is publicly available for the region around LNGS and for the relevant period of time. A single measurement (October 1, 2009) using miniaturized proportional counters of an air sample drawn underground close to the XENON100 detector exists, resulting in (1.33 ± 0.16) Bq/m^3 [39], or ^{85}Kr/^{nat}Kr = (2.11 ± 0.25) × 10^{-11} mol/mol in agreement with the expected average value.

In the following section we will discuss an *in situ* analysis technique to uniquely identify ^{85}Kr decays, quantify the krypton abundance during the investigated SRs, and compare the results to external measurements using a gas chromatographic system and a rare gas mass spectrometer (RGMS) [40].

4.1 Delayed coincidence analysis

^{85}Kr disintegrates by β^- emission to the ^{85}Rb ground state or, in 0.438 % of all cases, to its second excited level. The half-life of the latter is 1.015 μs. This decay mode offers a unique feature for ^{85}Kr identification. In more than 99 % of all cases the prompt β^- emission with endpoint energy of 173 keV is followed by a single 514 keV gamma. This clear, delayed coincidence signature allows for an *in situ* analysis of krypton concentrations in the XENON100 detector despite the tiny branching ratio and low statistics. Energy levels, branching ratios and half lives are taken from [11].

A set of basic cuts is applied in order to reject electronic noise and to ensure data quality, closely following the procedure outlined in [10]. We require a twofold PMT coincidence level for both the largest and next-to-largest S1 signals, as well as a minimum width of both the S1 waveforms. In addition, no light must be seen by the PMTs observing the LXe volume outside of the TPC (veto volume) in coincidence with the two S1 signals. Background events due to increased electronic noise in SR2 and SR3 are also removed. Finally, we require that at least one S2 signal be identified in each recorded event trace.

^{85}Kr delayed coincidence events are selected by requiring that the largest S1 (S1$_\gamma$) follows the next-to-largest S1 (S1$_\beta$) within a time window of 0.5–4.9 μs. The acceptance of this criterion is 67.5 %. In addition, we demand that the reconstructed S1$_\gamma$ and S1$_\beta$ energies fall within amply defined energy ranges: for the gamma interaction this is three times the detector resolution (taken from [5]) around the expected value, i.e., from 330–698 keV. The maximal accepted S1$_\beta$ energy is 219 keV, i.e., the decay's endpoint energy of 173 keV plus twice the detector's resolution.

Detector-specific acceptance losses for small energy S1$_\beta$ deposits are avoided by requiring signals to exceed 14 PE, corresponding to 5.8 keV [41]. The acceptance of the latter condition is computed to be 91.7 %, using the β-Fermi-Function and the GEANT4 implementation thereof [42–44]. Poisson-like fluctuations in S1$_\beta$ that affect the transformation from energy to S1 are negligible compared to the remaining uncertainties and ignored in the following. ^{212}BiPo events originating from the ^{220}Rn decay chain (see Sec. 3) close to or on the PTFE wall that encloses the TPC constitute the background. These events are successfully removed by requiring that the sum of all identified S2 signals, i.e., the ones from the β-particle and the γ-particle, fall within the expected energy region of 514–687 keV. Conservatively, the region is enlarged by five times the S2 energy resolution.

We use the energy and interaction-type dependent S1 light yield and S2 gain to convert the energy ranges into S1 and S2 light signals. In SR1, the statistics in ^{85}Kr events is sufficiently high in order to determine both the S1 light yield at 514 keV$_\gamma$ and the S2 gain at 514 keV$_\gamma$ + 48 keV$_\beta$. The latter corresponds to the S2 sum signal of the monoenergetic γ-particle and the β-electron with an average energy of 48 keV. For our purpose, we can assume the S1 light yield and S2 gain are constant throughout the three SRs investigated [8]. Finally, we use NEST [45], evaluated at 0.5 kV/cm similar to the XENON100 drift field, and the measured light yield at 122 keV, to convert the upper bound of our acceptance window for β particles into an S1 value.

To convert the number of identified delayed coincidence events into a krypton concentration (always given in mol/mol), we have to account for the lifetime, the amount of xenon, the cut acceptances of (61.7 ± 2.0) % in total, and the relative isotopic abundance of ^{85}Kr. For simplicity, we assume 2 × 10^{-11} mol/mol for the latter and resume the discussion in the context of induced uncertainties at the end of this section.

4.2 Results and discussion

Figure 5 shows the event distributions inside the TPC for the three SRs. Drawn in black are events passing all data selection criteria. Plotted in red are the events that pass all criteria except for the condition on the S2 sum. They are clearly clustered close to the PTFE wall enclosing the TPC, while the former (black events) are distributed throughout the TPC. For large radii, however, a reduced acceptance for events passing all selection criteria becomes obvious. We attribute this to a 514 keV γ-ray's mean free path of roughly 2 cm in liquid xenon [46]. Close to the wall these γ-rays can exit the TPC undetected and we lose the characteristic pattern
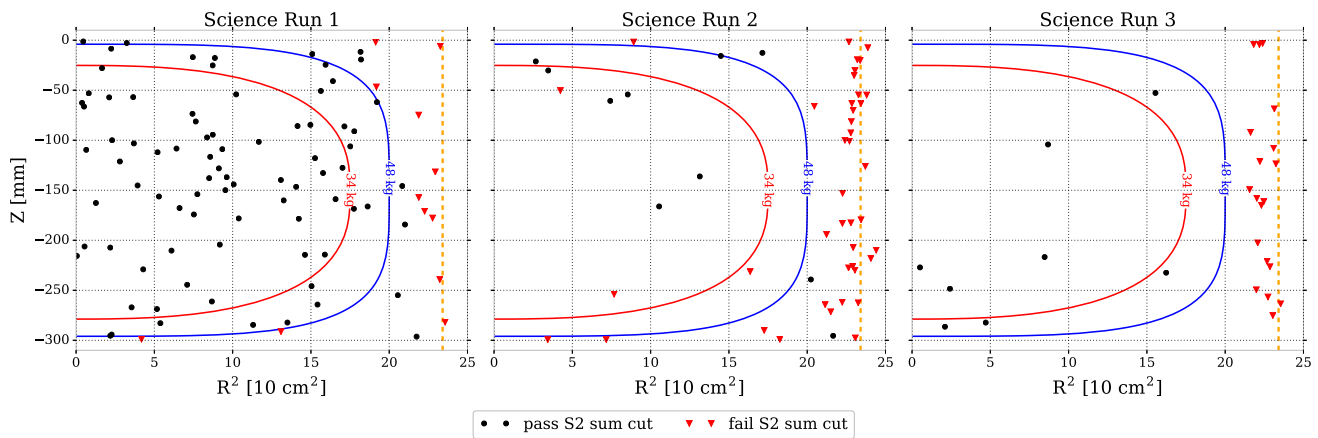
Fig. 5 Observed event distributions for all three SRs. Displayed in black are events passing all cuts. Shown in red are those events that pass all selection cuts except for the condition on the S2 sum. See text for details. The red (34 kg) and blue (48 kg) contours indicate the two fiducial volumes used in the publications of the three SRs [8,23,47]. Dashed lines indicate the TPC radius

Table 2 Overview of the ^{nat}Kr concentration measurements that were performed during the three SRs using mass spectrometry

Period	Date	^{nat}Kr/Xe (ppt)
SR1	02 Jun 2010	340 ± 60
SR2	17 Nov 2011	13.8 ± 2.4
SR3	14 Dec 2012	0.71 ± 0.24
	09 Jan 2013	0.95 ± 0.22
	21 Oct 2013	8.7 ± 1.5
	22 Dec 2013	11.1 ± 1.9

Table 3 Result of the delayed coincidence study for the three SRs and considering three different fiducial volumes (FV). The number of tagged events is converted into a krypton concentration (DC). The concentrations can be compared to the corresponding SR-averaged off-line measurements (RGMS). See text for details

Period	FV (kg)	Events (1)	^{nat}Kr/Xe (ppt)	
			DC	RGMS
SR1	34	54	370^{+60}_{-50}	340 ± 60
	48	74	360^{+50}_{-40}	
	62	83	310^{+40}_{-30}	
SR2	34	5	15^{+10}_{-7}	11.0 ± 1.7
	48	7	15^{+8}_{-6}	
	62	10	17^{+7}_{-5}	
SR3	34	4	18^{+14}_{-9}	6.3 ± 1.0
	48	8	25^{+13}_{-9}	
	62	8	20^{+10}_{-7}	

of the ^{85}Kr delayed coincidence. Fitting an exponential decay to the time delay between S1$_\beta$ and S1$_\gamma$, we find $T_{1/2} = 1.08(^{+0.18}_{-0.14})\,\mu s$ and $T_{1/2} = (0.32 \pm 0.04)\,\mu s$ for the events passing and failing the S2 sum condition, respectively. This supports the hypothesis that the former (black events) indeed are due to ^{85}Kr, while the latter (red events) are caused by the ^{212}BiPo delayed coincidence.

Table 2 lists all ^{nat}Kr measurements that were performed off-line with the RGMS setup using gas samples drawn from the purification loop of XENON100. In this loop, about 5 slpm of xenon are continuously evaporated from the liquid xenon phase. Due to this large mass flow, we assume the Kr concentrations of these gaseous samples to represent the liquid xenon target. Employing the model describing the time evolution of the krypton concentration from [13] and using the available RGMS measurements, we compute the run-averaged krypton concentrations of (340 ± 60) ppt, (11.0 ± 1.7) ppt and (6.3 ± 1.0) ppt for SR1 to SR3, respectively. Along with the RGMS-derived concentrations, Table 3 lists the number of identified delayed coincidence events and the resulting krypton concentrations (^{nat}Kr/Xe DC) found in the three SRs in the full TPC and two smaller fiducial vol-

umes. As discussed above, the chance to miss a delayed coincidence event increases with radius due to 514 keV gammas escaping the TPC undetected. To account for this, we consider the innermost fiducial volume (34 kg) only, where we find 370^{+60}_{-50} ppt (SR1), 15^{+10}_{-7} ppt (SR2) and 18^{+14}_{-9} ppt (SR3), in good agreement with the average concentrations derived from the RGMS measurements. Limited statistics prevails in the uncertainties of the delayed coincidence method. For example, in SR2, we select only 5 events in 7.6 td of exposure. Comparing the measurements of SR1 where statistics is most favorable, we find that the gas samples drawn from the liquid in fact represent the entire xenon target. However, there is a small indication of higher concentrations from the delayed coincidence analysis in SR2 and SR3, i.e., we compute probabilities of 0.058 (0.30) for finding 4 (5) or more events in SR3

Table 4 Estimates for the average ER background induced by the ^{222}Rn chain and ^{85}Kr (below 100 keV, before applying ER/NR discrimination). Values are inferred from different measurements. Only delayed coincidence values for the 34 kg fiducial volume are used, as they are affected the least by acceptance losses as outlined in Sec. 4.2

Source	Meas.	Induced ER rate [mDRU]		
		SR1	SR2	SR3
^{222}Rn	^{222}Rn	1.392 ± 0.012	1.865 ± 0.012	1.981 ± 0.012
	^{218}Po	1.189 ± 0.012	1.514 ± 0.009	1.711 ± 0.009
	^{214}BiPo	0.719 ± 0.017	0.951 ± 0.015	1.070 ± 0.015
^{85}Kr	DC	14^{+2}_{-2}	$0.6^{+0.4}_{-0.3}$	$0.7^{+0.5}_{-0.4}$
	RGMS	13 ± 2	0.43 ± 0.07	0.25 ± 0.04

(SR2) based on the corresponding RGMS-estimated concentrations. This hints at a background gaining more importance with reduced krypton concentration and increased exposure times by, for example, random coincidences due to altered noise conditions [8]. Alternatively, underestimating the abundance of ^{85}Kr that entered the detector through the air leaks in SR2 and SR3 could cause the surplus in events observed in the delayed coincidence analysis. In contrast to SR1, where the krypton was introduced in a short period of time for which we have a direct measurement of the ^{85}Kr/^{nat}Kr ratio, plumes arriving from the two nearest reprocessing plants La Hague, France, and Sellafield, England, could alter the abundance of ^{85}Kr for SR2 and SR3. We account for such an effect by averaging the ^{85}Kr activity concentration in ambient air monitored by the German Federal Office for Radiation Protection (BfS) [48] at Mount Schauinsland close to Freiburg, Germany, during the relevant periods of time. We find correction factors of +10, +30 and +50% with respect to our initial assumption of ^{85}Kr/^{nat}Kr = 2×10^{-11} mol/mol for SR1 to SR3, respectively. The resulting krypton concentrations are 340^{+60}_{-50} ppt, 12^{+8}_{-5} ppt and 12^{+9}_{-6} ppt, increasing the probabilities for the observed number of delayed coincidences to 0.17 (0.50) in SR3 (SR2). We assume this estimate to serve as a conservative upper limit only. The distance from the dominant sources La Hague and Sellafield to the monitoring station at Mount Schauinsland is only half of the distance to the underground laboratories. Increased ^{85}Kr concentrations due to reprocessing cycles are supposed to be reduced at LNGS. In fact, simulations suggest variations in central Italy to be only on the order of 0.5 Bq/m^3 [49]. Yet, for future experiments a local ^{85}Kr monitoring station is desirable to reduce this large systematic uncertainty.

5 Summary and conclusions

In this work, we presented techniques for selecting decays of the radon (^{222}Rn) and thoron (^{220}Rn) chains and those of ^{85}Kr. These methods allow us to estimate the contributions of the involved nuclei to the ER background and to study the distribution of background sources within the LXe target. Furthermore, they provide complementary values to those gained via direct measurements of the ^{222}Rn emanation rate and the concentration of natural krypton in the xenon target.

Background rates are given in units of differential rate (mDRU = 1×10^{-3} events/(kg day keV)). Monte Carlo studies [50], combined with the assumption of ^{85}Kr/^{nat}Kr = 2×10^{-11} mol/mol, yield conversion factors of 0.029 mDRU/(μBq/kg) and 0.039 mDRU/ppt to relate ^{222}Rn and ^{nat}Kr concentrations to ER rates, respectively. The ^{220}Rn chain has not been simulated due to ^{222}Rn and its daughters being more abundant as observed in data. The contribution of the ^{222}Rn chain can be estimated by using the observed ^{222}Rn rates. In the XENON100 science runs covered by this work, the xenon purity was affected by three air leaks of different leak rates. Consequently, we divide the radon-induced ER background into a constant pedestal driven by emanation and a variable offset due to ^{222}Rn leaking into the detector. In most parts of SR1, we do not observe a variable component due to external radon and infer the pedestal ER rate to be 1.4 mDRU. In SR2 (SR3) we find the variable offset to account for 0.5 mDRU (0.6 mDRU) on average. This corresponds to 35–40% of the total ^{222}Rn-induced ER background.

However, as we explained in Sec. 3.3, this overestimates the induced ER background because of plate-out effects. With ^{214}Pb being the most relevant β-emitter and ER background source of the chain [3], the actual ER background is smaller, assuming that the discrepancies between the decay rates arise mostly due to plate-out. We find the background index reduced to 86 % (50 %) if we take ^{218}Po (^{214}BiPo) rates to assess the effective activity concentration. Table 4 lists the radon contribution to the ER background using the different assumptions.

ER background from ^{85}Kr can be estimated via both RGMS and delayed coincidence measurements. While the RGMS measurements are more precise than the delayed coincidence measurements, we have to account for systematic

uncertainties in the ^{85}Kr/^{nat}Kr ratio. Delayed coincidence measurements suffer from limited statistics, especially in SR2 and SR3, but constitute a direct measurement of the ^{85}Kr concentration which does not rely on any assumption for the krypton ratio.

Based on the analysis procedures detailed in this work, we can quantify the amount of air that entered through the leaks by means of the two tracers radon and krypton. In all cases, we find the ^{85}Kr-based estimate to be a factor of approximately two lower than the one from ^{222}Rn. From measurements with a spiked ^{222}Rn source, we know that within only two hours radon homogeneously admixes throughout the entire LXe inventory [19]. The agreement between *in situ* delayed coincidence and external RGMS measurements suggests that we do not miss a significant fraction of krypton in the liquid xenon target. To resolve the apparent tension, we conclude that krypton is enriched in the gaseous part of the detector beyond the expected value of ~ 10 [51].

The contribution of ^{85}Kr in SR1 is (14 ± 2) mDRU – one order of magnitude larger than ^{222}Rn. Krypton removal by cryogenic distillation results in ^{222}Rn being dominant in SR2 and SR3. For instance in SR2, ^{222}Rn and ^{85}Kr contribute 29 % and 11 % to the total ER background, respectively. This emphasizes the necessity to understand and control the target-intrinsic backgrounds radon and krypton and, in particular, it outlines the importance of radon screening and dedicated material selection campaigns complemented by online radon removal techniques for current and future liquid noble gas experiments like nEXO [52], DarkSide-20k [53], LZ [54], XENON1T, XENONnT and DARWIN [55].

References

1. E. Aprile, T. Doke, Rev. Mod. Phys. **82** (2010), arXiv:0910.4956
2. P. Agnes et al. [DarkSide], Phys. Rev. D **93**, 8 (2016) Addendum: Phys. Rev. D **95**, 6 (2017), arXiv:1510.00702
3. E. Aprile et al. [XENON1T], JCAP **1604**, 4 (2016), arXiv:1512.07501
4. A. Dobi et al., [EXO], Nucl. Instrum. Meth. A **659**, 1 (2011). arXiv:1106.1812
5. E. Aprile et al., [XENON100], Astropart. Phys. **35**, 9 (2012). arXiv:1107.2155
6. D. S. Akerib et al. [LUX], Nucl. Instrum. Meth. A **704** (2013), arXiv:1211.3788
7. X. Cao et al. [PandaX], Sci. China Phys. Mech. Astron. **57** (2014), arXiv:1405.2882
8. E. Aprile et al. [XENON100], Phys. Rev. D **94**, 12 (2016), arXiv:1609.06154
9. B.A. Dolgoshein et al., JETP Lett. **11**, 351 (1970)
10. E. Aprile et al. [XENON100], Astropart. Phys. **54** (2014), arXiv:1207.3458
11. M.-M. Bé et al., *Table of Radionuclides vol. 1/2/4/7* (Bureau International des Poids et Mesures), http://www.nucleide.org/DDEP_WG/DDEPdata.htm. Accessed 07 Nov 2016
12. E. Aprile et al., [XENON100], Astropart. Phys. **35**, 2 (2011). arXiv:1103.5831
13. E. Aprile et al. [XENON100], Phys. Rev. Lett. **118**, 10 (2017), arXiv:1701.00769
14. E. Aprile et al. [XENON100], Phys. Rev. D **95**, 7 (2017), arXiv:1611.03585
15. G. Alimonti et al., [Borexino], Astropart. Phys. **8**, 3 (1998)
16. H. Gómez [SuperNEMO], Nucl. Instrum. Meth. A **718**, 52 (2013)
17. M. Weber, PhD thesis, Ruprecht-Karls-Universität Heidelberg (2013), http://hdl.handle.net/11858/00-001M-0000-0013-F898-0
18. J. Gaiser, PhD thesis, SLAC Stanford (1982), http://www.slac.stanford.edu/cgi-wrap/getdoc/slac-r-255.pdf
19. E. Aprile et al. [XENON100], Eur. Phys. J. C **77**, 6 (2017), arXiv:1702.06942
20. E. Aprile et al., Phys. Rev. Lett. **97**, 8 (2006). arXiv:astro-ph/0601552
21. D. Cichon, Master thesis, Ruprecht-Karls-Universität Heidelberg (2015), http://hdl.handle.net/11858/00-001M-0000-0029-1F55-6
22. A. Bradley et al. [LUX], Phys. Procedia **61** (2015)
23. E. Aprile et al., [XENON100], Phys. Rev. Lett. **107**, 13 (2011). arXiv:1104.2549
24. S. Lindemann, PhD thesis, Ruprecht-Karls-Universität Heidelberg (2013), http://hdl.handle.net/11858/00-001M-0000-0014-BD63-F
25. T. Sasaki, Y. Gunji, T. Okuda, JNST **41**, 2 (2004)
26. S. Lindemann and H. Simgen, G. Zuzel, AIP Conf. Proc. **1338** (2011)
27. J. B. Albert et al. [EXO-200], Phys. Rev. C **92**, 4 (2015), arXiv:1506.00317
28. H.M. Araujo et al., [ZEPLIN-III], Astropart. Phys. **35**, 495 (2012). arXiv:1104.3538
29. M. Clemenza et al., Eur. Phys. J. C **71** (2011)
30. A.I. Bolozdynya et al., Nucl. Instrum. Meth. A **579**, 1 (2007)
31. K. Abe et al., [XMASS], Astropart. Phys. **31**, 4 (2009). arXiv:0809.4413
32. Z. Wang et al., Rev. Sci. Instrum. **85**, 1 (2014)
33. E. Aprile et al. [XENON], Eur. Phys. J. C **77**, 5 (2017), arXiv:1612.04284
34. K.J.P. Schroeder, W. Roether, *Releases of Krypton-85 and Tritium to the Environment and Tritium to Krypton-85 Ratios as Source Indicators* (International Atomic Energy Agency, Vienna, 1975)
35. K. Winger et al., J. Environ. Radiat. **80**, 2 (2005)
36. H.H. Loosli, B.E. Lehmann, W.M.J. Smethie, *Environmental Tracers in Subsurface Hydrology* (Kluwer Academic Publishers, Dordrecht, 2000)
37. J. Bieringer et al., Appl. Radiat. Isot. **67**, 5 (2009)
38. X. Du et al., Geophys. Res. Lett. **30**, 20 (2003). arXiv:physics/0311118

39. S. Lindemann, Diploma thesis, Ruprecht-Karls Universität Heidelberg (2009), http://hdl.handle.net/11858/00-001M-0000-0011-738A-4

40. S. Lindemann, H. Simgen, Eur. Phys. J. C **74** (2014), arXiv:1308.4806

41. E. Aprile et al. [XENON100], Phys. Rev. Lett. **115**, 9 (2015), arXiv:1507.07748

42. P. Venkataramaiah et al., J. Phys. G **11**, 3 (1985)

43. S. Agostinelli et al., GEANT4. Nucl. Instrum. Meth. A **506**, 3 (2003)

44. S. Hauff et al., IEEE Trans. Nucl. Sci. **60**, 4 (2013). arXiv:1307.0996

45. M. Szydagis et al., JINST **8** (2013), arXiv:1307.6601

46. J. H. Hubbell, S. M. Seltzer, *X-Ray Mass Attenuation Coefficients* (National Institute of Standards and Technology), http://physics.nist.gov/PhysRefData/XrayMassCoef/ElemTab/z54.html. Accessed 07 Nov 2016

47. E. Aprile et al., [XENON100], Phys. Rev. Lett. **109**, 18 (2012). arXiv:1207.5988

48. German Federal Office for Radiation Protection (BfS) (2014), http://nbn-resolving.de/urn:nbn:de:0221-2016091514109

49. J. O. Roß, PhD thesis, Universität Hamburg (2010), http://hdl.handle.net/11858/00-001M-0000-0027-A54A-F

50. E. Aprile et al., [XENON100], Phys. Rev. D **83**, 8 (2011). arXiv:1101.3866

51. S. Rosendahl et al., Rev. Sci. Instrum. **86**, 11 (2015)

52. J. B. Albert *et al.* [nEXO], arXiv:1710.05075

53. C. E. Aalseth et al. [DarkSide-20k], arXiv:1707.08145

54. B. J. Mount et al. [LZ], arXiv:1703.09144

55. J. Aalbers et al. [DARWIN], JCAP **1611** (2016), arXiv:1606.07001